

Defect Cluster Morphologies in W from Collision Cascades: Results Comparing Five Inter-atomic potentials

M Warriar^{a,b}, U Bhardwaj^a

^aComputational Analysis Division, BARC, Visakhapatnam, Andhra Pradesh, India – 530012

^bHomi Bhabha National Institute, Anushaktinagar, Mumbai, Maharashtra, India – 400094

Abstract

The size and morphology of defect clusters formed during primary damage play an important part in the subsequent evolution of the micro-structure of irradiated materials. Molecular dynamics (MD) simulations of collision cascades in W have been carried out using five interatomic potentials (IAP) including the quantum accurate machine learned (ML) spectral neighbor analysis potential (WSNAP), the ML based tabGAP potential and three embedded atom method (EAM) based potentials. A total of 3500 MD simulations with the primary knock-on atoms (PKA) having energies 5, 10, 20, 50, 75, 100 and 150 keV were carried out. The PKA are launched in hundred random directions at each of the PKA energies to obtain statistically valid results. Analysis using CSaransh, a web based tool to analyze a large collision cascade database, was carried out to obtain the number of defects (individual and in clusters), the defect cluster morphologies, the defect cluster size distributions and the number of sub-cascades formed. It is seen that $\langle 111 \rangle$ clusters dominate across all the inter-atomic potentials (IAP), except for the WSNAP potential. The WSNAP potential shows significantly higher number of C-15 like rings across all PKA energies. The WSNAP potential also shows a higher fraction of in-cluster vacancies. It is also seen that the stiffness and range of IAP do not affect the number of defects, defect clustering or vacancy clusters, but shows a tendency to form more sub-cascades for PKA energies less than 60 keV.

Keywords: collision cascades, irradiation, defects, defect clusters, molecular dynamics (MD), LAMMPS, Tungsten

1. Introduction

Molecular dynamics (MD) has been widely used to study the primary damage in materials due to irradiation ([1] and references therein). Irradiation by energetic ions or neutrons creates energetic primary knock-on atoms (PKA) which gives rise to a collision cascade. The collision cascade causes a large number of atoms to displace from their lattice positions. The cascade of displaced atoms peaks within a pico-sec and recombines with local vacancies to create the "primary damage" state with interstitials, vacancies and defect clusters. The primary damage evolves with time due to further irradiation, transport of defects, their interactions with each other and with pre-existing micro-structures in the material [2–4].

Several researchers have studied the effect of IAP on collision cascades and on the surviving defects at the end of a cascade. Byggmästar et al. simulating collision cascades in Fe, have shown that the range over

Email addresses: manoj.warrier@gmail.com (M Warriar), haptork@gmail.com (U Bhardwaj)

which the pair potential is stiffened to account for interactions at small separations between atoms can be adjusted so as to reproduce the measured experimental displacement energy (E_D) for the material [5]. They also show that the damage evolution at high doses depends on the formation and stability of defect clusters, which is dictated by the equilibrium part of the interatomic potential. Sand et al. have carried out two different degrees of pair-potential stiffening [6] of an embedded atom method (EAM) potential developed by Marinica et al. for W [7]. They have compared the results for collision cascades from these potentials with three other IAP. They show the variation of the number of self interstitial atoms (SIA) with the Frenkel-pair formation energy, vacancy migration energy, displacement energy and the ratio of stiffness to range as defined in [8]. They also show the effect of stiffening on the distribution of defects in the cascade. Becquart et al. have studied the effect of seven empirical IAP of W and five empirical IAP of Fe on collision cascades [9, 10]. [9] shows clear correlations between the threshold displacement energy (TDE), replacement collision sequences (RCS) and the quasi static drag (QSD) along $\langle 110 \rangle$ direction of these bcc crystals and recommend that during the pair potential stiffening procedure, care must be taken to correctly reproduce the interactions of atoms moving in the $\langle 110 \rangle$ direction. In [10] they study the effects of potential stiffening on cascade properties like number of single interstitials and vacancies, fraction interstitials and vacancies and their maximum sizes and the correlation of these with cascade morphology, defined by sphericity and volume of the cascades.

Bhradwaj et al. have classified the defect clusters observed in primary damage based on the morphology including orientation of the defect clusters [11]. MD simulations of collision cascades with three different EAM based IAP have shown similar classes of defect clusters [12]. However, there exists a large variation in the number of defect clusters in the various classes obtained with the three IAP. The stability, transport and interactions of the defect clusters depend upon their size and morphology. For example, the stability of $\langle 100 \rangle$ defect clusters depend upon their size and internal morphology [13]. It is reasonable to assume that the same holds true for defect clusters belonging to other classes. Since the stability, transport and interaction of the defect clusters can influence the micro-structure evolution, it is essential to know which IAP results in the right quantities of defect morphologies that match experiments. Unfortunately there exist no experimental results of primary damage that can identify the various morphologies of defect clusters and quantify them at these resolutions. Moreover, for comparison with experiments, in-situ experiments need to be carried out, since the primary damage state which results at the end of the collision cascade simulations evolves with time and at higher doses of radiation, multiple cascades can also occur at the same location.

In the past decade, quantum mechanical density functional theory (DFT) calculations have been used to generate the total energy, force on each atom and stresses for a large database of atomic configurations, and machine learning (ML) methods are being used to construct IAP [14–16]. Wood and Thompson have developed a spectral neighbor analysis potential (WSNAP) for tungsten which aims to improve the accuracy, quality and realism of the MD predictions in order to approach the accuracy of DFT [17]. Bygmästar et al. have developed a tabulated Gaussian approximation potential (tabGAP) for Mo-Nb-Ta-V-W alloys which shows high accuracy when applied to multicomponent alloys, but is less accurate for single element simulations [18]. In this study we compare the results of defects formed during MD simulations of collision cascades in tungsten using the ML based IAP (WSNAP and tabGAP) with that from three EAM based IAP, namely DND-BN [19], MS [6], and JWPot [20]. PKA at 5, 10, 20, 50, 75 and 150 keV, are launched in 100 random directions within the tungsten crystal, leading to a total of 3500 MD simulations. Our earlier study, wherein we have explored these three non-ML potentials [12], was on a much smaller dataset in terms of PKA energies explored and also in the number of random PKAs launched at each energy. We present results on the number of defects (single and in clusters), the maximum sizes of defect clusters, the morphology of the

defect clusters and their variation with IAP.

In the next section, a description of the MD simulations of collision cascades and a brief discussion of the five potentials that are compared is presented. The results for the number of defects, their cluster size distribution, the defect cluster morphologies and the number of defects in various classes of defect morphologies, the number of sub-cascades formed, etc. will be presented in the third section, followed by a discussion of the results and our conclusions.

2. Description of the MD Simulations of collision cascades

The Large Scale Atomic/Molecular Massively Parallel Simulator (LAMMPS) was used to carry out the MD simulations [21]. Different cubic simulation boxes of the sizes specified in Table.1, were initially subjected to a NPT relaxation for 10 ps at 300 K and 0 bar pressure using periodic boundary conditions (pbc) along all the three directions. The time step used in the NPT simulations is one fs. The simulation box sizes are chosen such that the cascade occurs within a region excluding the outermost three unit cells. This is subsequently verified during post-processing of the collision cascade wherein except for a negligible fraction of channeling events, all cascades occur inside the defined box.

Post relaxation, a central atom in the simulation box is identified as the PKA. 100 NVE simulations of collision cascades are then carried out at each PKA energy by directing the PKA towards 100 random points on a unit sphere with the PKA at its center, with the initial velocity of the PKA corresponding to the PKA energy. Electronic stopping is considered as a frictional term as described in [22]. The outermost unit cells of the simulation box are fixed and the adjacent two unit cells to the outermost cells are temperature controlled at 300 K. Variable time stepping is used along with pbc along all three directions during the NVE simulations which last upto 20 ps. The positions of atoms displaced above a threshold value and their velocity components are output at a specified frequency during the simulations. At the end of the simulation, all atom positions and their potential energy are output for post-processing.

Table 1: The simulation cell size and number of atoms used at each PKA energy in the MD simulations

S.No	PKA Energy (keV)	Simulation Size	No. of Atoms
1	5	$50 \times 50 \times 50$	250000
2	10	$75 \times 75 \times 75$	843750
3	20	$85 \times 85 \times 85$	1228250
4	50	$100 \times 100 \times 100$	2000000
5	75	$125 \times 125 \times 125$	3906250
6	100	$150 \times 150 \times 150$	6750000
7	150	$200 \times 200 \times 200$	16000000

2.1. Brief description of the interatomic potentials used

The above described MD simulations were carried out using two ML based potentials, WSNAP [17] and tabGAP [18], and three EAM based potentials, DND-BN [19], MS (specifically the MS_h potential) [6] and JWPot [20]. Fig.1 shows the variation of the pair potential of the atoms as a function of their separation and Table.2 lists the main stiffening parameters of the five IAP. r_1 and r_2 are the distances over which the pair

potential of the original EAM potential are smoothly interpolated to the universal ZBL potential, R is the range, defined as the interatomic distance where the pair potential is 30 eV, and S is the stiffness, defined as the slope of the potential at R . The IAPs used are briefly described below so that the results may be compared in the context of the main aspects considered during the IAP construction.

Table 2: The pair potential stiffening parameters for the five IAP. In the second and third columns for the WSNAP and tabGAP potentials, ZBL and SC represent the pair potentials these two ML based potentials have been fitted to, with SC denoting a Screened Coulomb potential.

IAP	r1 (Å)	r2 (Å)	R (Å)	S	S/R (Å ⁻¹)
JW	1.39	2.6	1.4	-150	-107
DND-BN	1.1	2.25	1.3	-230	-177
MS	1.3	2.0	1.45	-137	-95
WSNAP	ZBL	ZBL	1.4	-145	-104
tabGAP	SC	SC	1.27	-223	-176

2.2. JW Potential

Juslin et al. added a short range modification to the Ackland-Thetford modification [23] of the Finnis-Sinclair W potential [24] (ATFSPot) thus improving the potential at distances where interstitials can form. This was done by smoothly interpolating the pair part of the ATFSPot to the ZBL potential [25] from a distance of $r_2=2.6$ Å, lesser than the nearest neighbor distance, to a point $r_1=1.39$ Å. Keeping r_2 less than the nearest neighbor distance ensured that the good match with bulk properties shown by the ATFSPot was retained whilst improving the potential where self interstitials could exist. It was shown that the modified potential (JW) compares with DFT results better than the ATFSPot does for formation energy of the $\langle 110 \rangle$ and $\langle 111 \rangle$ dumbbell and the octahedral self interstitials [20]. The modified potential also improves the match with the experimental value [26] of the threshold displacement energy E_D , which plays an important part creating displaced atoms in collision cascades. However the minimum and average values of E_D with the modified potential are 48 eV and 128 eV respectively, which is higher than the experimentally derived values of minimum 40-50 eV and an average of 80 eV. The bulk properties are same as the unmodified potential, which shows a 10% higher melting point than experiments.

2.3. DND-BN Potential

The DND-BN potential [19] was developed by modifying the EAM potential for W developed by Derlet, Nguyen-Manh and Dudarev [27] in order to correctly reproduce experimentally observed displacement energies. Both, the pair part, and the electron density part, were modified. The pair part was smoothly interpolated to the ZBL potential between the distances $r_1=1.1$ Å and $r_2=2.25$ Å, so that the repulsive part of the potential matches the ZBL potential at close approaches of atoms to each other. The electron density function was modified to correctly account for the contribution of the attractive electron d-states. The values of E_d with this potential are 41 eV along the $\langle 111 \rangle$ and $\langle 100 \rangle$ directions and 93 eV along the $\langle 110 \rangle$ direction, with an average of 84.5 eV. This closely matches the experimental values of a minimum of 40-50 eV and an average of 80 eV [26].

2.4. MS Potential

An EAM potential was developed by Marinica et al. [7] by fitting a database of experimentally measured properties and ab-initio data. Ab-initio formation energies of defects like (i) mono self-interstitial atom along

$\langle 110 \rangle$, $\langle 111 \rangle$, $\langle 100 \rangle$, (ii) mono self-interstitial atoms at octahedral and tetrahedral locations within the unit cell, (iii) mono-vacancy, and (iv) interatomic forces computed for random liquid configurations, were used as fitting data. Experimentally measured elastic constants C_{11} , C_{12} and C_{44} , lattice parameters and cohesive energies of the BCC structure, etc. were also used for the fitting. Four EAM potentials were developed by fitting the above data (EAM1, EAM2, EAM3 and EAM4), which were then validated by comparing with ab-initio calculated formation energies of defect clusters not used in the fitting, extended defects like surface energies, and basic properties of the $\langle 111 \rangle$ screw dislocation.

Sand et al. stiffened the EAM4 potential developed by Marinica, et al. [7] for two different degrees of stiffening, referred to as "soft" (MS_s) and "hard" (MS_h) [6]¹. MS_s smoothly interpolated between the pair potential of the EAM4 potential to the ZBL between $r_1=0.6 \text{ \AA}$ to $r_2=1.2 \text{ \AA}$, whilst the MS_h carried out the interpolation between $r_1=1.3 \text{ \AA}$ and $r_2=2.0 \text{ \AA}$. The displacement energies from the MS potential were 31, 51 and 45 eV along the $\langle 100 \rangle$, $\langle 110 \rangle$ and $\langle 111 \rangle$ directions.

2.5. WSNAP potential for W

The WSNAP potential was developed to obtain quantum level accuracy of tungsten potentials for simulation of plasma facing materials in fusion reactors [17]. It uses the bispectrum components of the 4D hyperspherical harmonics on the 3-sphere [29] to characterize atomic neighborhoods, and assumes a linear relationship between the atomic energy and the bispectrum components. The short range repulsive interactions between atomic cores is modelled using the ZBL potential. The training data consists of the total energies, force components on each atom and virial stresses calculated using density functional theory (DFT) corresponding to specified positions for various configurations of tungsten atoms. The configurations considered are (i) primitive cell deformations, (ii) BCC tungsten with a vacancy, (iii) free surfaces with various orientations, (iv) a sampling of DFT-MD of BCC crystal at 300 K, (v) isotopic compression and dilation of BCC, FCC, A15 and SC tungsten crystals, (vi) 27 configurations from a melted 54 atom supercell of tungsten, and (vii) $3 \times 3 \times 3$ BCC crystals with vacancy pairs ranging from nearest neighbor to 4th nearest neighbor positions.

2.6. tabGAP potential for W

Byggmästar et al. have shown that using simple low-dimensional two and three-body descriptors in a typical Gaussian approximation potential (GAP) outperformed using much higher order descriptors when fitting ML potentials for a high entropy alloy (Mo-Nb-Ta-V-W) system [18]. The two and three-body potential could be tabulated and evaluated easily using cubic spline interpolations, and therefore they refer to the potential as tabGAP. They used the two-body, three-body and a simple scalar many-body density descriptor based on the EAM to develop a potential that was not only more accurate, but also was much faster to evaluate. The repulsive pair potential at close distances of approach of the atoms was fitted to the screened coulomb potential. The training dataset consisted of various crystal and liquid structures with various alloy compositions, interstitials and vacancies, dimers and structures with short separations for fitting repulsions, etc. A detailed list of the fitted data is available in [18]. The authors state that the potential is not as accurate for individual elements as it is for the five element alloy the potential was developed for.

¹Contrary to the standard nomenclature, where the potential gradient is ∞ at the radius of the hard sphere and the sphere is said to be softer as the potential gradient decreases [28], in [6] the term "soft" is used for the higher gradient and "hard" for the lower gradient in the potential function. Following this, the same nomenclature is also used in [9, 10]. In this document we stick to the historical nomenclature due to it being physically motivated.

2.7. Post-processing

The outputs from 3500 MD simulations were analysed using the CSaransh post-processor [11, 30–32] which can be used to post-process large databases of MD XYZ output. The XYZ output here refers to the X, Y and Z coordinates of all the atoms in the MD simulation at the end of the collision cascade. CSaransh identifies the defects, their clusters and classifies them based on their orientation and internal morphology. Details of the defect identification and classification of defect structures are described in [11, 31]. The sub-cascades identification in CSaransh uses a density based clustering method on the primary damage [32]. The results from this analysis are in agreement with that from existing algorithms that identify sub-cascades at the peak of the cascade.

3. Results

The distribution of the number of defects for all the five potentials are shown in Fig.2. It is seen that there is a broad distribution in the number of defects at all PKA energies for all the IAP. The arc-DPA [33] values for tungsten is also plotted for reference. At higher PKA energy the width of the distribution is larger. Note also that the IAP which have higher mean number of defects at low PKA energies do not maintain this status at higher PKA energies. The JW and MS potentials show a good quantitative and qualitative match with each other whilst the tabGAP potential shows the least number of defects at all PKA energies.

The fraction of defects in clusters for the different IAP is shown as a function of PKA energy in Fig.3. Note that there is a clear hierarchy for the clustered fraction of defects at almost all PKA energies, with the DND-BN potential showing the maximum fraction and the MS potential showing the least. At PKA energy of 150 keV the fraction of defects in clusters varies from 0.65 to 0.8, whilst at 5 keV PKA energy the fraction varies from 0.45 to 0.55. There is no trend for the fraction of defects in clusters with the stiffness and range values of the pair potential when we compare Fig.3 with Table.2.

The vacancy cluster size distributions from the five IAP are shown in Fig.4 for PKA energies 5-20 keV, 50-75 keV and 100-150 keV. It is seen that the WSNAP potential shows the largest vacancy cluster sizes. The percentage of vacancies in clusters are shown as a function of PKA energy in Fig.5. The standard deviation from the 100 random directions are also shown in the figure. It is seen that the WSNAP potential shows the largest percentage of vacancies in cluster at PKA energies greater than 20 keV. Note that there is no trend with stiffness and range for the size of vacancy clusters. The WSNAP, MS and the JW potential have similar values of S and R, but only the WSNAP potential shows larger vacancy sizes and larger percentage of vacancies in cluster.

Fig.6 shows the six basic defect cluster classes seen in the primary damage state in all the 5 IAP using graph based analysis [11]. They are listed below along with the ascii symbols used to define them:

1. $1/2\langle 111 \rangle$ dislocations and clusters (ascii symbol ||-111),
2. $\langle 100 \rangle$ dislocations and clusters with $\langle 111 \rangle$ and $\langle 110 \rangle$ crowdions bounding them (ascii symbol ||!),
3. mixed $1/2\langle 111 \rangle$, $\langle 110 \rangle$, $\langle 100 \rangle$ dislocations (ascii symbol ||//),
4. C15 like rings (ascii symbol @),
5. C15 like rings with $\langle 111 \rangle$ clusters (ascii symbol ||@), and
6. small random arrangement of crowdions (ascii symbol #).

The fraction of defects in each of the six morphologies are shown in Fig.7. There is an extra cluster type, \parallel -110, added in the figure since a few such defect clusters were also observed during analysis. It is seen that most of the defects are in \parallel -111 type. More than 80 % of the defects are of this type in JW and tabGAP potentials and around 60 % in MS and DND-BN potentials. The WSNAP potential however has around 15 % of its defects as \parallel -111 and 40 % as \parallel @ which consists of bigger $\langle 111 \rangle$ component with small ring components. Most of the defects in the WSNAP potential are either of type @ (35 %) or \parallel @ (40 %). The MS potential is the only other potential that shows a moderate number of @ (20 %) or \parallel @ (5%). This could be a consequence of both these potentials being trained on liquid configurations of W [6, 17]. The distribution of the sizes of the defect clusters are shown in Fig.8. The \parallel -100 also form big dislocations in addition to $\parallel\parallel\parallel$ and $\langle 111 \rangle$ dislocations. The \parallel @ also has large sizes, mostly due to the \parallel component. The WSNAP potential shows large complex @ structures.

A density based clustering mechanism was developed to identify the sub-cascades from the primary damage state at the end of a collision cascade [32]. This mechanism shows good agreement with methods that use the peak state of the cascade to identify sub-cascades [10]. Fig.9 shows the number of sub-cascades at each of the PKA energies for the five IAP. The tabGAP potential shows a marginal tendency to form more sub-cascades while the WSNAP potential shows a marginal tendency to form fewer sub-cascades. Note that the stiffer potentials (see Tab.2), tabGAP and DND-BN show more tendency at PKA energies less than 50 keV, to form sub-cascades compared to the other three IAP. However, at PKA energies greater than 60 keV, the tabGAP potential retains this property, but the DND-BN potential does not.

4. Discussion

The changes in micro-structure of irradiated materials depends on both, the primary damage, and the evolution of the damage. The change in micro-structures occurs by defect migration and interaction with each other and with pre-existing defects like grain-boundaries, etc. From Fig.2 it is seen that the number of defects from the various potentials fall generally within the same range irrespective of S or S/R for PKAs launched in 100 random directions. Overall these results support the conclusion from [5, 34] that the choice of IAP does not majorly affect the number of defects, provided the stiffening parameters are reasonable. The above statement does not encompass the MS_s potential from Sand et al [6] which has stiffness, $S=-552$ and range, $R=-502$ compared to the potentials explored in this work which have S within the range -137 to -230 and a S/R values in the range -95 to -177. The MS_s potential is much stiffer than the ZBL potential and the pair interaction potentials from two DFT simulations considering the 6s and 5d orbitals as valence electrons in one case and including the 5p electrons also as valence electrons in the other (Fig.1 from [6]). The MS_s potential however illustrates the effect of an extremely stiff pair potential on a cascade. It is also known that the stiffness of an IAP affects cascade properties like volume of cascade and sphericity [6, 10].

The various IAP agree on the number of defects created, but not on the fraction of defects in clusters. It is seen from Fig.3 that the fraction of defects in clusters vary by as much as 20-40 % depending on the IAP chosen as has been observed by other researchers [10]. They also show similar basic classes of defect clusters which have been classified based on their orientation and morphology [31], but the fraction of clusters in the various classes are different as is seen from Fig.7 and Fig.8. The results for the fraction of defects in clusters shown in Fig.3, fraction and sizes of defect clusters in various morphologies do not show a dependence on S or S/R for the range of S and S/R explored in this work.

The clustering of defects depend on both, the distribution of displaced atoms at the peak of the cascade and their subsequent interaction with each other. One of the factors affecting the distribution of displaced atoms at the peak is the stiffness of the IAP. Their subsequent interaction to form clusters depends upon the behaviour of the IAP at intermediate distances which is decided by the defect configurations data the IAP have been trained on. For example note the prevalence of rings (@ and ||@) in the results from the SNAP and MS potential (trained on liquid configurations) compared to the other IAP. This indicates that the defect configurations data the IAP have been trained on affects the clustering. The stability of the defect clusters depend not only on their size, but also their internal morphology [13]. The presence of sessile morphologies with high transition energy could be nucleation sites for the glissile defects during the evolution of the micro-structure and their signatures may show up in HRTEM experiments. To identify these, further studies of the migration and interaction of defect morphologies need to be carried out. Therefore identifying defect cluster morphologies for various IAP and comparing with experiments will be helpful in validating the IAP and making better predictions.

5. Conclusions

The primary damage characteristics due to collision cascades in tungsten are explored using five different IAP for hundred randomly directed PKA in the energy range of 5 keV to 150 keV. The following results stand out from the analysis:

- It is seen that the number of defects formed, the fraction of defects in clusters and the number of sub-cascades do not have any correlation to the S and S/R ratios of the IAP.
- The fraction of defects in clusters shows a variation of at most 20 % for the different IAP, but there is no trend with S and S/R of the IAP.
- Most of the IAP show defect clusters that fall into six classes based on their morphology and orientation, with four of the IAP producing maximum number of ||-111 defect clusters. The exception is the quantum accurate WSNAP potential which shows a majority of @ and ||@ kind of clusters. This is probably due to liquid configurations being part of the training set used to construct the WSNAP potential.
- The WSNAP potential also shows the largest vacancy clusters, whilst the other IAP all show similar vacancy sizes. Again the vacancy sizes do not have any correlation to the S and S/R ratio.
- Stiffer potentials at PKA energies below 50 keV tend to form more sub-cascades.

From the above observations it is clear that the S and S/R ratio do not affect the number of defects, defect clustering or vacancy clusters for the range of S and S/R values explored by our choice of IAP. The IAP chosen affects the fraction of defects in clusters and the morphology of the clusters. The quantum accurate machine learnt potential for, SNAP, shows a very different cluster morphology and percentage of vacancies in clusters compared to the other IAP. Note that IAP with extreme stiffening of the pair potential like the MS_s in [6] have not been used in this study.

Acknowledgements

We acknowledge the HPC team at CAD for 24×7 HPC maintenance and for support in installing and running LAMMPS.

References

- [1] R. Stoller, 1.11 - primary radiation damage formation, in: R. J. Konings (Ed.), *Comprehensive Nuclear Materials*, Elsevier, Oxford, 2012, pp. 293 – 332. doi:<https://doi.org/10.1016/B978-0-08-056033-5.00027-6>.
- [2] K. Nordlund, Historical review of computer simulation of radiation effects in materials, *Journal of Nuclear Materials* 520 (2019) 273–295. doi:<https://doi.org/10.1016/j.jnucmat.2019.04.028>. URL <https://www.sciencedirect.com/science/article/pii/S0022311518314703>
- [3] C. Domain, C. Becquart, L. Malerba, Simulation of radiation damage in fe alloys: an object kinetic monte carlo approach, *Journal of Nuclear Materials* 335 (1) (2004) 121 – 145. doi:<http://dx.doi.org/10.1016/j.jnucmat.2004.07.037>.
- [4] R. Stoller, S. Golubov, C. Domain, C. Becquart, Mean field rate theory and object kinetic monte carlo: A comparison of kinetic models, *Journal of Nuclear Materials* 382 (2) (2008) 77 – 90, *microstructural Processes in Irradiated Materials*. doi:<http://dx.doi.org/10.1016/j.jnucmat.2008.08.047>.
- [5] J. Byggmästar, F. Granberg, K. Nordlund, Effects of the short-range repulsive potential on cascade damage in iron, *Journal of Nuclear Materials* 508 (2018) 530–539. doi:<https://doi.org/10.1016/j.jnucmat.2018.06.005>. URL <https://www.sciencedirect.com/science/article/pii/S0022311518305166>
- [6] A. Sand, J. Dequeker, C. Becquart, C. Domain, K. Nordlund, Non-equilibrium properties of interatomic potentials in cascade simulations in tungsten, *Journal of Nuclear Materials* 470 (2016) 119–127. doi:<https://doi.org/10.1016/j.jnucmat.2015.12.012>. URL <https://www.sciencedirect.com/science/article/pii/S0022311515303810>
- [7] M.-C. Marinica, L. Ventelon, M. R. Gilbert, L. Proville, S. L. Dudarev, J. Marian, G. Bencteux, F. Willaime, Interatomic potentials for modelling radiation defects and dislocations in tungsten, *Journal of Physics: Condensed Matter* 25 (39) (2013) 395502. doi:[10.1088/0953-8984/25/39/395502](https://doi.org/10.1088/0953-8984/25/39/395502). URL <https://dx.doi.org/10.1088/0953-8984/25/39/395502>
- [8] C. S. Becquart, A. Souidi, M. Hou, Relation between the interaction potential, replacement collision sequences, and collision o *Phys. Rev. B* 66 (2002) 134104. doi:[10.1103/PhysRevB.66.134104](https://doi.org/10.1103/PhysRevB.66.134104). URL <https://link.aps.org/doi/10.1103/PhysRevB.66.134104>
- [9] C. S. Becquart, A. De Backer, P. Olsson, C. Domain, Modelling the primary damage in fe and w: Influence of the short range i *Journal of Nuclear Materials* 547 (2021) 152816. doi:<https://doi.org/10.1016/j.jnucmat.2021.152816>. URL <https://www.sciencedirect.com/science/article/pii/S0022311521000398>
- [10] A. De Backer, C. S. Becquart, P. Olsson, C. Domain, Modelling the primary damage in fe and w: influence of the short-range i *Journal of Nuclear Materials* 549 (2021) 152887. doi:<https://doi.org/10.1016/j.jnucmat.2021.152887>. URL <https://www.sciencedirect.com/science/article/pii/S0022311521001100>
- [11] U. Bhardwaj, A. E. Sand, M. Warrier, Graph theory based approach to characterize self interstitial defect morphology, *Computational Materials Science* 195 (2021) 110474. doi:<https://doi.org/10.1016/j.commatsci.2021.110474>. URL <https://www.sciencedirect.com/science/article/pii/S0927025621001993>

- [12] U. Bhardwaj, A. E. Sand, M. Warriar, Comparison of sia defect morphologies from different interatomic potentials for collision Modelling and Simulation in Materials Science and Engineering 29 (6) (2021) 065015. doi:10.1088/1361-651X/ac095d. URL <https://dx.doi.org/10.1088/1361-651X/ac095d>
- [13] U. Bhardwaj, A. E. Sand, M. Warriar, Stability of $\{100\}$ dislocations formed in w collision cascades, Journal of Nucl. Mater. 569 (2022) 153938.
- [14] J. Behler, Perspective: Machine learning potentials for atomistic simulations, The Journal of Chemical Physics 145 (17) (2016) 170901. arXiv:https://pubs.aip.org/aip/jcp/article-pdf/doi/10.1063/1.4966192/13889426/170901\1\1_online doi:10.1063/1.4966192. URL <https://doi.org/10.1063/1.4966192>
- [15] Y. Mishin, Machine-learning interatomic potentials for materials science, Acta Materialia 214 (1) (2021) 116980. doi:10.1016/j.actamat.2021.116980. URL <https://doi.org/10.1016/j.actamat.2021.116980>
- [16] V. L. Deringer, A. P. Bartók, N. Bernstein, D. M. Wilkins, M. Ceriotti, G. Csányi, Gaussian process regression for materials and molecules, Chemical Reviews 121 (16) (2021) 10073–10141, pMID: 34398616. arXiv:<https://doi.org/10.1021/acs.chemrev.1c00022>, doi:10.1021/acs.chemrev.1c00022. URL <https://doi.org/10.1021/acs.chemrev.1c00022>
- [17] M. A. Wood, A. P. Thompson, Quantum-accurate molecular dynamics potential for tungsten (2017). arXiv:1702.07042.
- [18] J. Byggmästar, K. Nordlund, F. Djurabekova, Modeling refractory high-entropy alloys with efficient machine-learned interatomic potentials, Physical Review B 104 (10). doi:10.1103/physrevb.104.104101. URL <https://doi.org/10.1103/physrevb.104.104101>
- [19] C. Björkas, K. Nordlund, S. Dudarev, Modelling radiation effects using the ab-initio based tungsten and vanadium potentials, Nuclear Instruments and Methods in Physics Research Section B: Beam Interactions with Materials and Atoms 267 (18) (2009) 3204 – 3208, proceedings of the Ninth International Conference on Computer Simulation of Radiation Effects in Solids. doi:<http://dx.doi.org/10.1016/j.nimb.2009.06.123>.
- [20] N. Juslin, B. Wirth, Interatomic potentials for simulation of helium bubble formation in tungsten, Journal of Nuclear Materials 432 (1) (2013) 61 – 66. doi:<https://doi.org/10.1016/j.jnucmat.2012.07.023>.
- [21] A. P. Thompson, H. M. Aktulga, R. Berger, D. S. Bolintineanu, W. M. Brown, P. S. Crozier, P. J. in 't Veld, A. Kohlmeyer, S. G. Moore, T. D. Nguyen, R. Shan, M. J. Stevens, J. Tranchida, C. Trott, S. J. Plimpton, LAMMPS - a flexible simulation tool for particle-based materials modeling at the atomic, meso, and continuum scales, Comp. Phys. Comm. 271 (2022) 108171. doi:10.1016/j.cpc.2021.108171.
- [22] H. Hemani, A. Majalee, U. Bhardwaj, A. Arya, K. Nordlund, M. Warriar, Inclusion and validation of electronic stopping in the open source lammps code (2020). arXiv:2005.11940.

- [23] G. J. Ackland, R. Thetford, An improved n-body semi-empirical model for body-centred cubic transition metals, *Philosophical Magazine A* 56 (1) (1987) 15–30. arXiv:<https://doi.org/10.1080/01418618708204464>, doi:10.1080/01418618708204464. URL <https://doi.org/10.1080/01418618708204464>
- [24] M. W. Finnis, J. E. Sinclair, A simple empirical n-body potential for transition metals, *Philosophical Magazine A* 50 (1) (1984) 45–55. arXiv:<https://doi.org/10.1080/01418618408244210>, doi:10.1080/01418618408244210. URL <https://doi.org/10.1080/01418618408244210>
- [25] J. F. Ziegler, J. P. Biersack, The stopping and range of ions in matter, in: *Treatise on Heavy-Ion Science*, Springer, 1985, pp. 93–129.
- [26] F. Maury, M. Biget, P. Vajda, A. Lucasson, P. Lucasson, Frenkel pair creation and stage i recovery in w crystals irradiated near threshold, *Radiation Effects* 38 (1-2) (1978) 53–65. arXiv:<https://doi.org/10.1080/00337577808233209>, doi:10.1080/00337577808233209. URL <https://doi.org/10.1080/00337577808233209>
- [27] P. M. Derlet, D. Nguyen-Manh, S. L. Dudarev, Multiscale modeling of crowdion and vacancy defects in body-centered-cubic t. *Phys. Rev. B* 76 (2007) 054107. doi:10.1103/PhysRevB.76.054107. URL <https://link.aps.org/doi/10.1103/PhysRevB.76.054107>
- [28] A. M. Patrick, D. J. Tildesley, *Computer simulation of liquids* 2nd ed.
- [29] Hosseinbor, A. Pasha, et al., 4d hyperspherical harmonic (hyperspharm) representation of multiple disconnected brain subcortical structures, *Medical image computing and computer-assisted intervention: MICCAI, International Conference on Medical Image Computing and Computer-Assisted Intervention* 16 (Pt 1) 598–605.
- [30] U. Bhardwaj, H. Hemanu, M. Warriar, N. Semwal, K. Ali, A. Arya, Saransh : Software suite to study molecular dynamics simulations of collision cascades, *Journal of Open Source Software* 4(41) (2019) 1461. doi:<https://doi.org/10.21105/joss.01461>.
- [31] U. Bhardwaj, A. E. Sand, M. Warriar, Classification of clusters in collision cascades, *Computational Materials Science* 172 (2020) 109364. doi:<https://doi.org/10.1016/j.commatsci.2019.109364>. URL <https://www.sciencedirect.com/science/article/pii/S0927025619306639>
- [32] U. Bhardwaj, M. Warriar, Identifying subcascades from the primary damage state of collision cascades (2023). arXiv:2306.04975.
- [33] K. Nordlund, S. J. Zinkle, A. E. Sand, F. Granberg, et al., Improving atomic displacement and replacement calculations with physically realistic damage models, *Nature Communications* 9 (2018) 1084.
- [34] D. Terentyev, C. Lagerstedt, P. Olsson, K. Nordlund, J. Wallenius, C. Becquart, L. Malerba, Effect of the interatomic potential on the features of displacement cascades in $\alpha - fe$: A molecular dynamics study, *Journal of Nuclear Materials* 351 (1) (2006) 65–77, proceedings of the Symposium on Microstructural Processes in Irradiated Materials. doi:<https://doi.org/10.1016/j.jnucmat.2006.02.020>. URL <https://www.sciencedirect.com/science/article/pii/S0022311506000675>

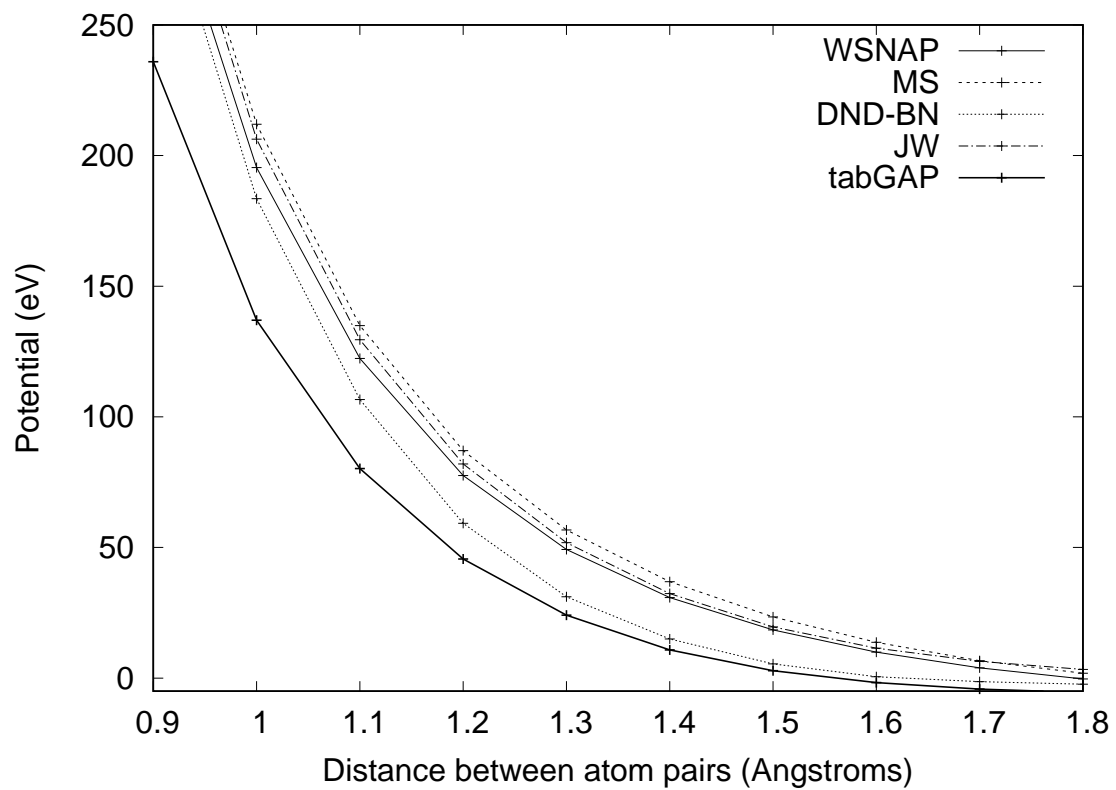


Figure 1: Total potential energy of a pair of atoms as a function of the distance between them.

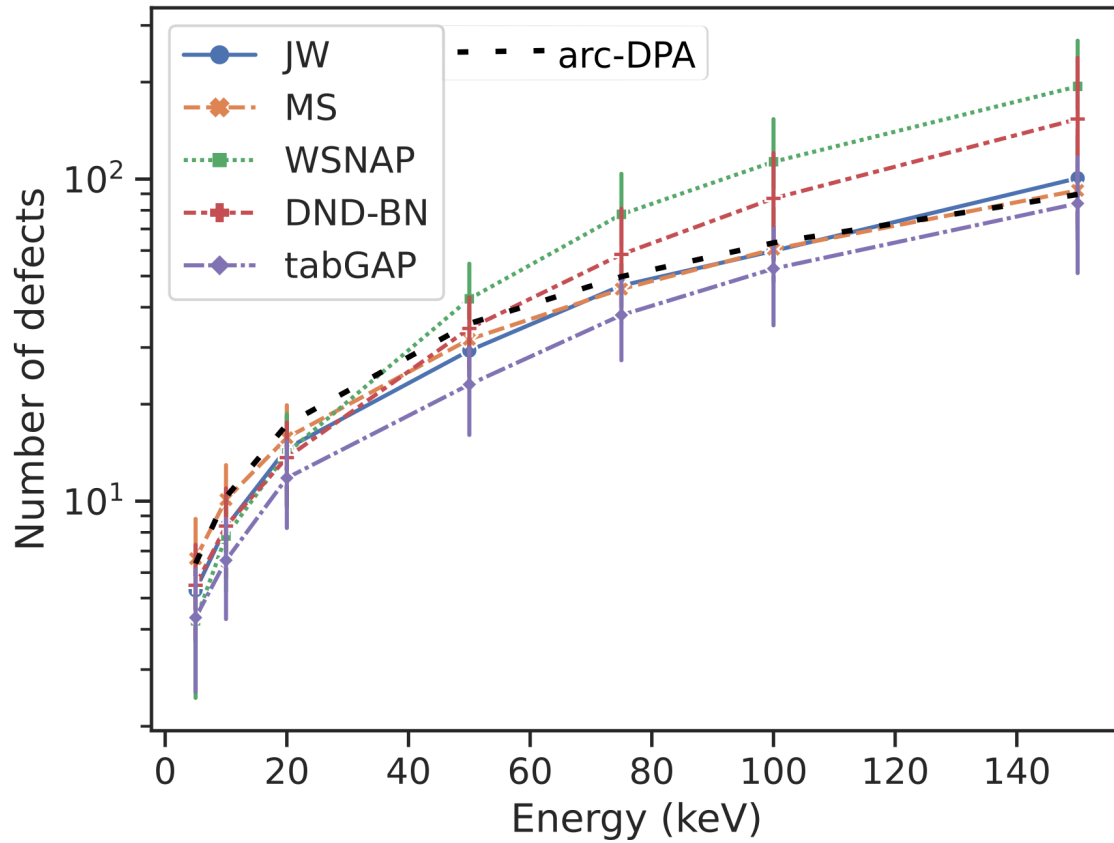


Figure 2: Plot of the number of defects from the five IAP as a function of PKA energy for the PKAs launched in 100 random directions. The standard deviation is also shown in the figure.

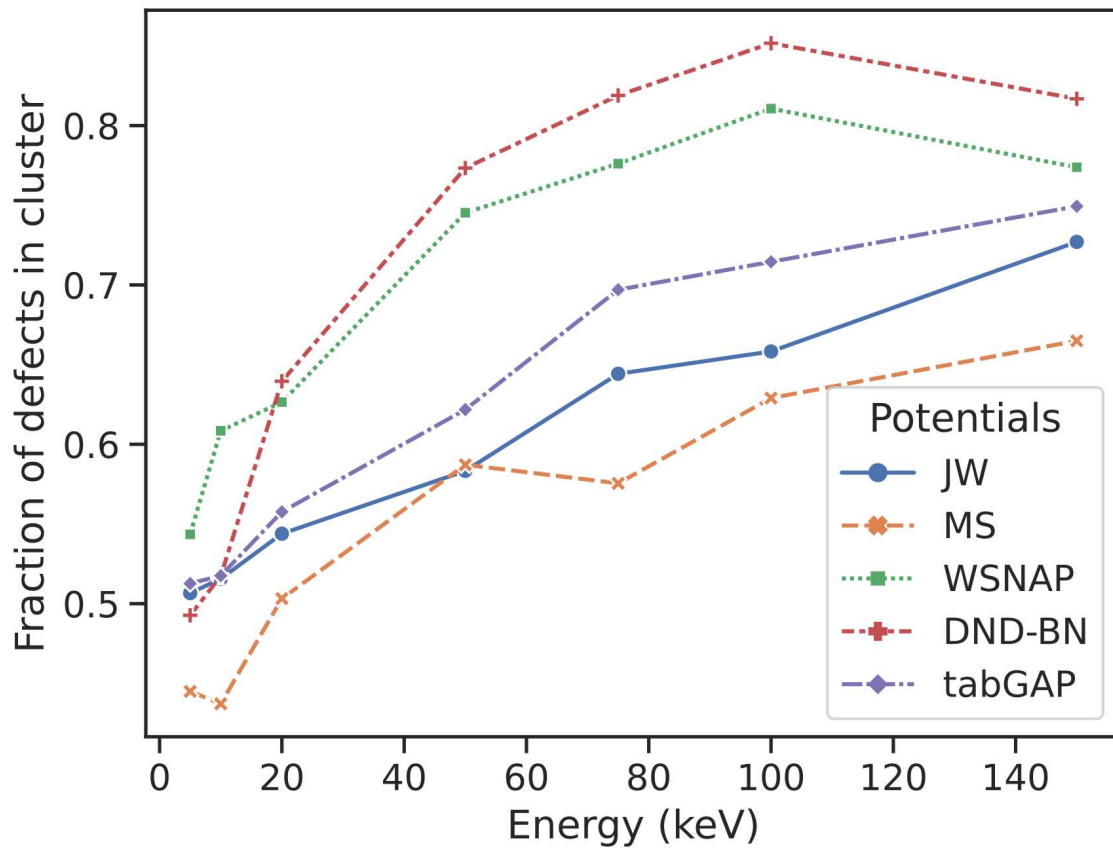


Figure 3: Fraction of defects in clusters as a function of PKA energy for the five Interatomic Potentials.

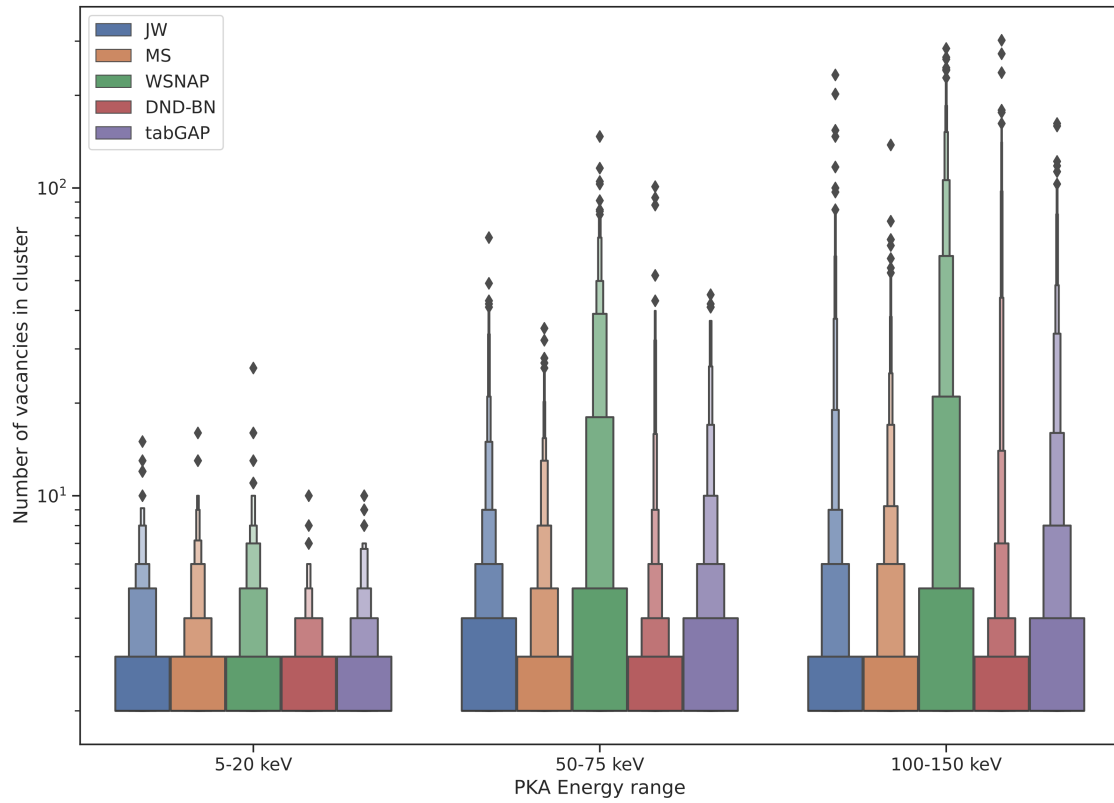


Figure 4: Box plots of the size of vacancy clusters from the 5 IAP for three different sets of PAK energies, namely 5-20 keV, 50-75 keV and 100-150 keV.

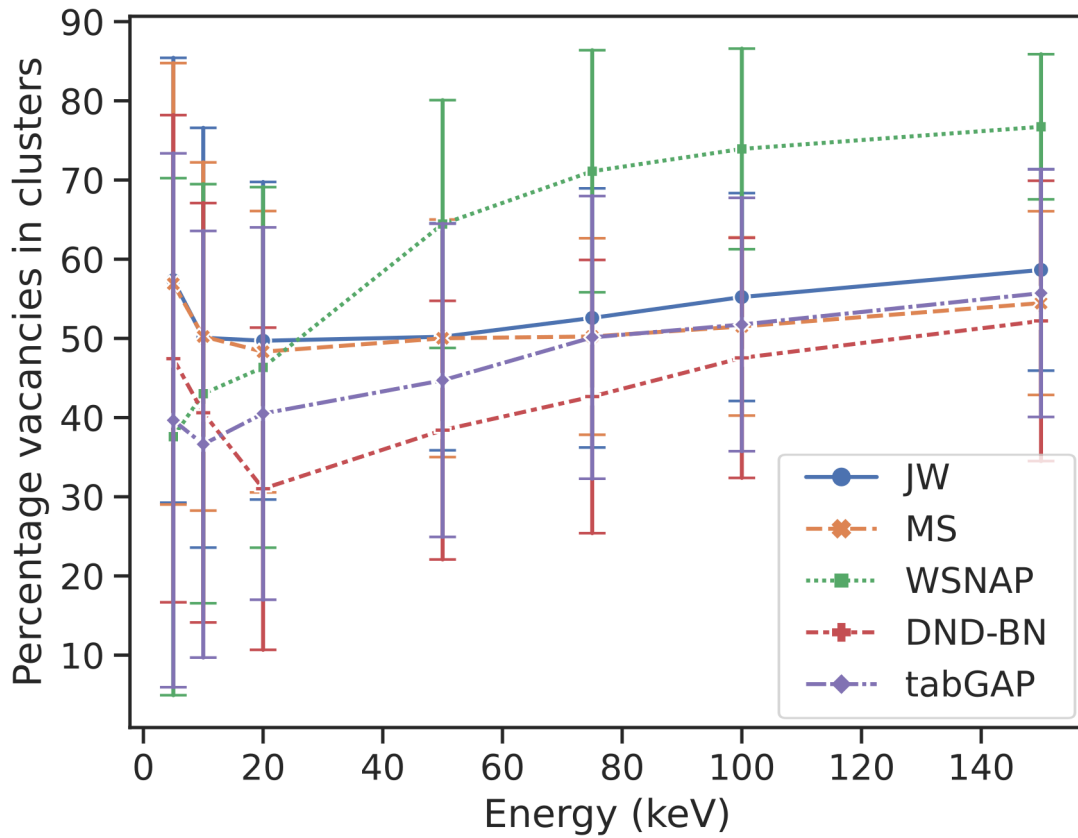


Figure 5: In cluster vacancies

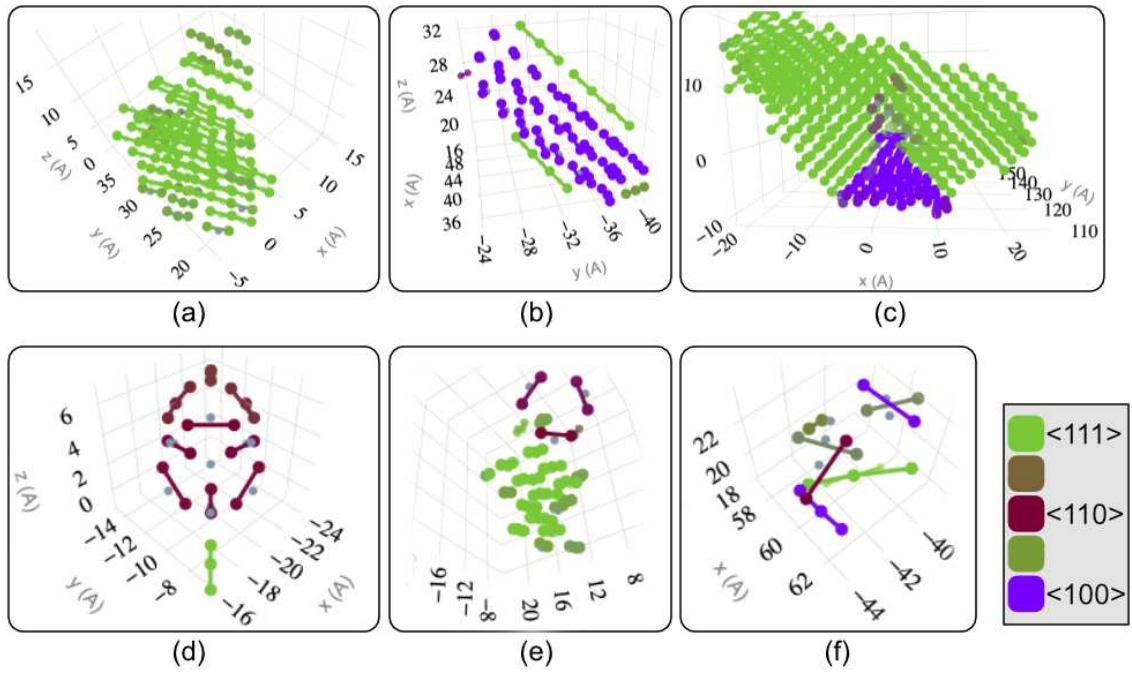


Figure 6: The six classes of defects seen in W which are observed in the primary damage at the end of collision cascade simulations. Note that these are present irrespective of the interatomic potentials used [11].

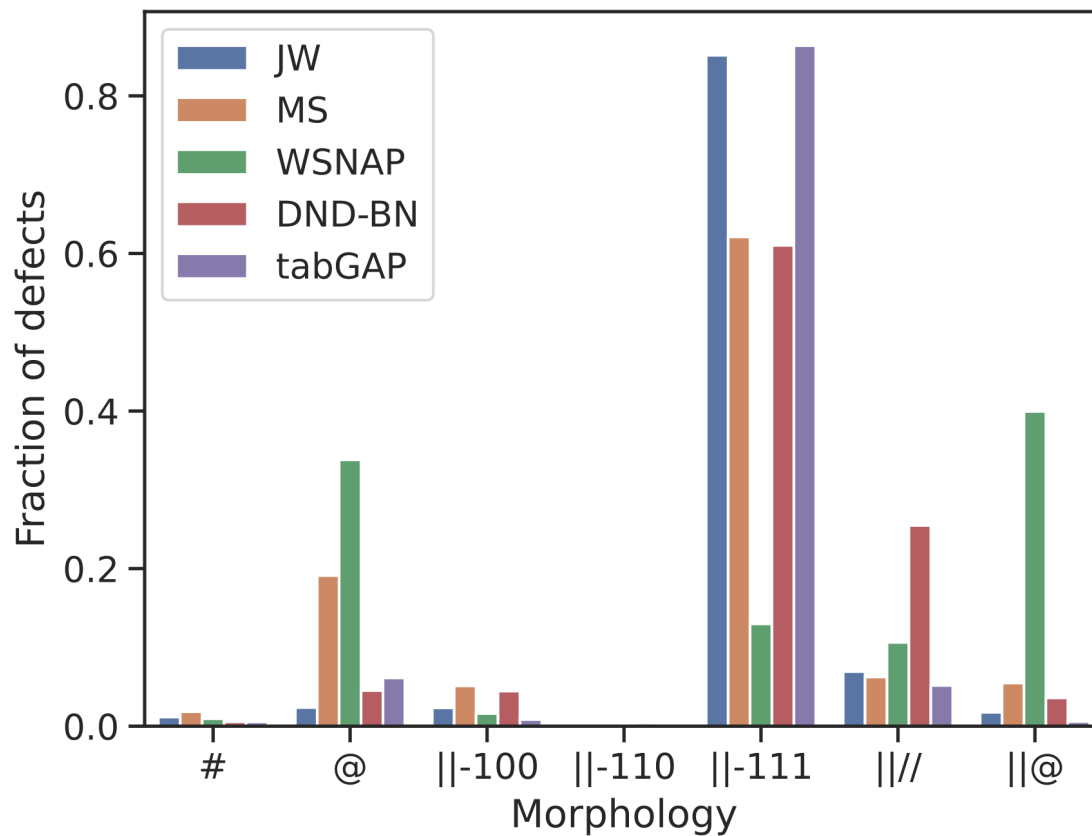


Figure 7: The Fraction of defects in each of the morphologies for five Interatomic Potentials.

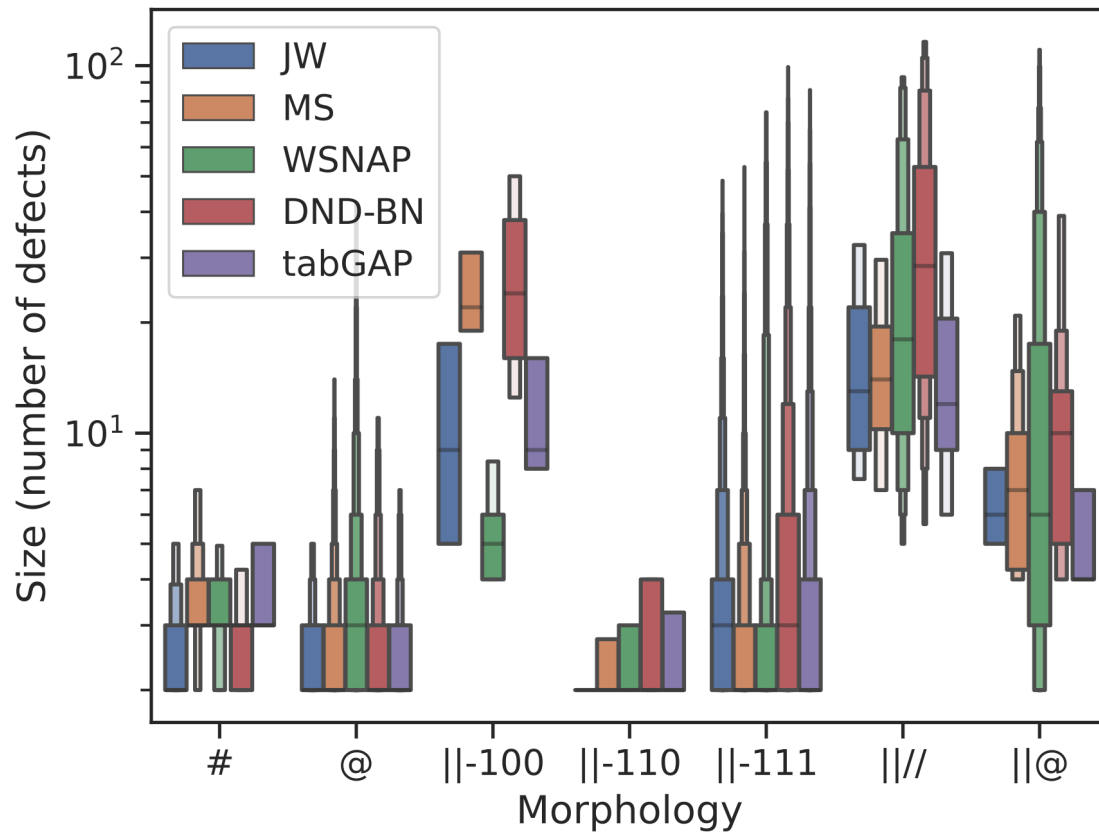


Figure 8: The defect size distribution in each of the morphologies for five Interatomic Potentials.

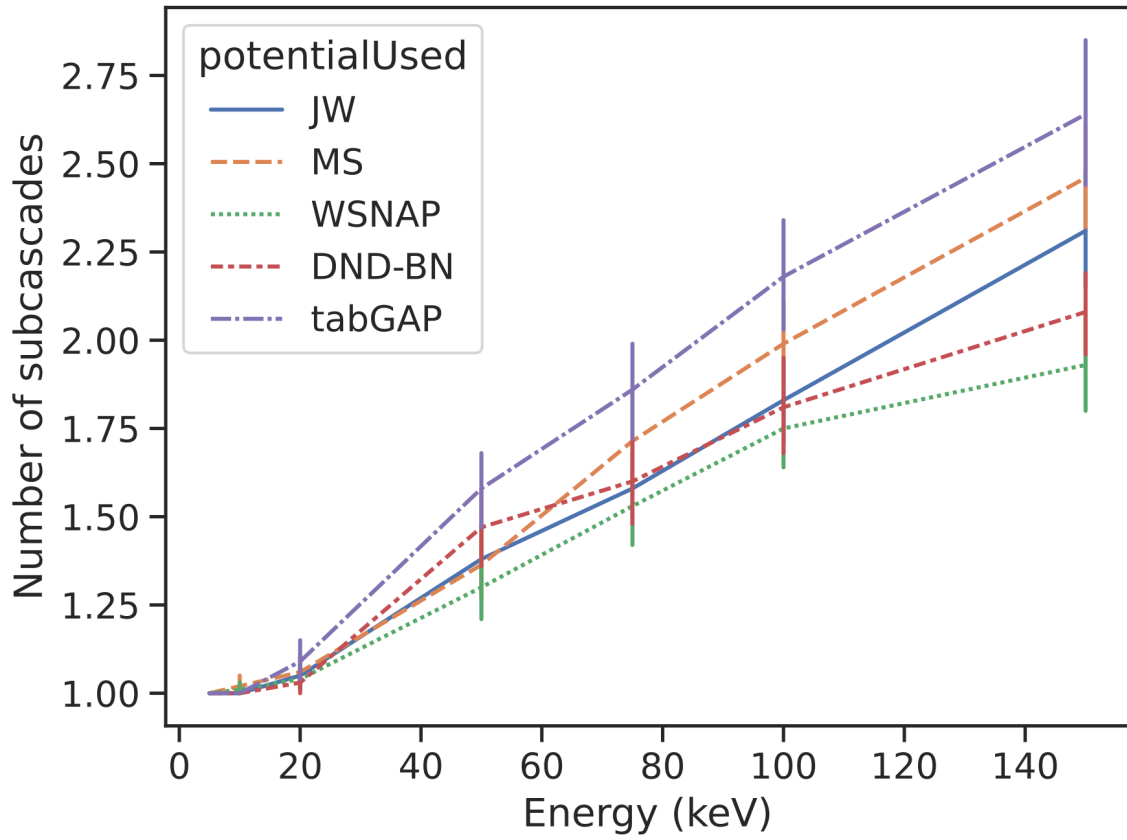


Figure 9: The number of subcascades as a function of the PKA energy.